

## PAPER

CrossMark  
click for updatesCite this: *RSC Adv.*, 2016, 6, 35365

# Efficient visible light photocatalysis and tunable photoluminescence from orientation controlled mesoporous Si nanowires†

Ramesh Ghosh<sup>a</sup> and P. K. Giri<sup>\*ab</sup>

Herein, orientation controlled growth of single crystalline mesoporous Si nanowires (NWs) by Ag assisted etching of Si(100) and Si(111) wafers and its visible light photocatalysis efficiencies have been studied. By choosing different orientations of the starting Si wafer and concentration of etchants, we have tuned the morphology of Si NWs and achieved straight, bent, kinked and zigzag Si NWs. High resolution FESEM and TEM imaging reveals that the Si NWs are decorated with ultra-small Si nanocrystals (NCs) of arbitrary shape due to the lateral etching of the NWs. A strong broad-band visible to near-infrared (NIR) photoluminescence (PL) in the range 1.4–2.4 eV is observed from these Si NWs/NCs at room temperature. Our studies reveal that the quantum confinement of carriers in Si NCs and the nonbridging oxygen hole center (NBOHC) defects in the SiO<sub>x</sub> layer both contribute to the broad visible-NIR PL. In addition to the efficient PL emission, the metal assisted chemical etching (MACE) grown Si NWs exhibit excellent photocatalytic degradation of methylene blue under visible light illumination. The Si–H bonds present on the surface of the Si NWs/NCs facilitate the photocatalytic activity by efficient separation of the photogenerated e–h pairs. Our studies reveal that the MACE grown vertically aligned Si NWs behave as a stable photocatalyst for up to five cycles of catalysis. It is found that with the increase in the concentration of HF during etching, PL intensity systematically decreases while the photocatalytic efficiency increases with the HF concentration due to the Si–H bonds. Our results open up the possibility of using Si NWs arrays in white light display applications as well as organic waste treatment and hydrogen production by photocatalytic water splitting.

Received 29th February 2016

Accepted 1st April 2016

DOI: 10.1039/c6ra05339d

[www.rsc.org/advances](http://www.rsc.org/advances)

## 1. Introduction

Over the past few decades, Si nanowires (NWs) have been attracting a great deal of attention in both basic scientific research and technological applications due to their unique physical and chemical characteristics.<sup>1–7</sup> Si NWs grown by metal assisted chemical etching (MACE) have been employed as an active component in various electronic and optoelectronic devices, *e.g.*, field effect transistors,<sup>6</sup> light emitting diodes,<sup>2</sup> solar cells,<sup>1</sup> sensors,<sup>4</sup> energy storage<sup>3</sup> and photochemical reactors<sup>5</sup> *etc.* The elucidation of the morphology controlled growth of single crystalline Si NWs is critical to understanding the fundamental physics of NWs to design and fabricate Si NWs based innovative nano-devices with tunable characteristics. Depending on size, morphology, doping and surface conditions, MACE grown Si NWs exhibit tunable visible-near infrared

(NIR) photoluminescence (PL) at room temperature (RT).<sup>8–18</sup> Earlier studies pointed out that the MACE grown Si NWs are often decorated with arbitrary shaped Si nanocrystals (NCs) due to the sidewall etching and the quantum confinement (QC) effect in Si NCs is primarily responsible for the broad visible PL.<sup>8,10,11,15,19</sup> However, strong influence of surface defects in the PL has been emphasized in some studies.<sup>20–24</sup> The as-grown Si NWs/NCs are often covered with a native oxide layer and non-bridging oxygen hole center (NBOHC) defects in the oxide matrix are reported to be responsible for the visible PL at RT.<sup>19,22–24</sup> Si NCs decorated Si NWs grown by MACE have shown excellent photocatalytic efficiency under visible light illumination.<sup>5,25–28</sup> MACE grown Si NWs exhibit high optical absorption, extremely low reflectance and tunable PL in the entire visible-NIR range. Earlier studies suggest that Si–H bonds present on the surface of Si NWs/NCs serve as the photoelectrochemical reaction centers during photodegradation.<sup>5,19,25,27</sup> In addition, ultralow reflection/broadband absorption over the entire visible range and the unaltered metal nanoparticles (NPs) during etching also contribute to the photocatalytic efficiency of MACE grown Si NWs/NCs.<sup>19,27</sup>

Over the past few years, MACE has emerged a promising and significant tool for rapid production of large area, aligned and

<sup>a</sup>Department of Physics, Indian Institute of Technology Guwahati, Guwahati-781039, India. E-mail: [giri@iitg.ernet.in](mailto:giri@iitg.ernet.in)

<sup>b</sup>Centre for Nanotechnology, Indian Institute of Technology Guwahati, Guwahati-781039, India

† Electronic supplementary information (ESI) available. See DOI: 10.1039/c6ra05339d

well controlled Si NWs.<sup>10,29–33</sup> Mostly Ag has been used as the noble metal catalysts for the growth of Si NWs by MACE. However, it is well known that the morphology of as-grown Si NWs depends on the etchant concentration, doping type, dopant concentration and the orientation of the Si NWs. Straight vertical Si NWs from Si(100) wafer and zigzag Si NWs from Si(111) have been observed by using different concentration of HF/H<sub>2</sub>O<sub>2</sub>.<sup>10,32,34</sup> However, to the best of our knowledge, the effect of the curved and zigzag morphology on the visible PL and photocatalytic activity of MACE grown Si NWs has not been reported. Further, the correlation between the photocatalytic and photoluminescence efficiencies for the Si NWs has not been addressed in the literature.

In this work, Si NWs have been synthesized by MACE of two different kinds of Si wafers, mainly Si(100) and Si(111) wafers using Ag as the noble metal catalyst and HF/H<sub>2</sub>O<sub>2</sub> as the etchants. Straight, bent, kinked and zigzag Si NWs have been achieved by changing the relative concentration of the etchants. As-grown Si NWs are decorated with self-grown Si NCs of different sizes and arbitrary shapes due to the side wall etching of Si NWs and it results in mesoporous Si NWs. The light emission characteristics of the Si NWs/NCs are investigated thoroughly. Photodegradation efficiency and recyclability of Si NWs/NCs as a photocatalyst under visible light irradiation were studied using methylene blue (MB) as a degrading agent. The effect of etchants concentration on the PL emission and photocatalytic efficiency is studied extensively and a correlation between these two phenomena is elucidated.

## 2. Experimental details

### 2.1. Synthesis of Si NWs

Si NWs were grown by the well-known MACE process using Si wafers at room temperature (RT). P-type Si(100) and Si(111) wafers with resistivity 0.01 and 0.001 Ω cm, respectively, were used as the starting material. The wafers were first cleaned by typical RCA cleaning process.<sup>10</sup> For the MACE of the cleaned Si wafers, we used a two-step process. In this process, first a thin

layer of Ag nanoparticles (NPs) was deposited on the Si wafers by dipping it in a solution containing 5.55 M HF and 0.015 M AgNO<sub>3</sub> for 5 seconds. Next, the as-deposited substrates were immersed in a solution containing HF and H<sub>2</sub>O<sub>2</sub> for 20 min at RT. Details of the wafer cleaning, Ag NPs deposition and the etching steps are provided in the ESI† (Section I). To study the effect of HF concentration on the morphology of Si NWs, the amount of HF is varied from 2 mL to 8 mL into an etching solution containing 2 mL H<sub>2</sub>O<sub>2</sub> (fixed) and 23 mL DI water (fixed). Samples grown using Si(100) wafer are labeled as group “S1”, while those grown with Si(111) are labeled as group “S2”. Depending on the relative concentration of HF keeping the concentration of H<sub>2</sub>O<sub>2</sub> and water constant, the samples are named as S1HF2, S1HF3 *etc.* Detailed descriptions of the samples are summarized in Table 1.

### 2.2. Characterization techniques

The morphology and the structure of the Si NWs were characterized using a field emission scanning electron microscope (FESEM) (Sigma, Zeiss) equipped with an energy-dispersive X-ray spectrometer (EDX) and a transmission electron microscope (TEM) (JEOL-JEM 2100) operated at 200 kV, respectively. For the compositional analysis, X-ray photoelectron spectroscopy (XPS) measurements were carried out using a PHI X-Tool automated photoelectron spectrometer (ULVAC-PHI Inc.) using Al K $\alpha$  X-ray beam (1486.6 eV) with a beam current of 20 mA. Carbon 1s spectrum was used for the calibration (284.8 eV) of the XPS spectra recorded for various samples.<sup>35</sup> The steady state PL spectrum was recorded using a 405 nm diode laser (Cube, Coherent) excitation with the help of a PL spectrometer (Horiba Jobin Yvon Fluoromax-4). Each spectrum was corrected for the detector response as a function of wavelength after background subtraction. Raman scattering measurement was carried out with a 514 nm Ar<sup>+</sup> laser excitation using a micro-Raman spectrometer (LabRAM HR-800, Jobin Yvon). The diffuse reflectivity of the samples was carried out using an ellipsometer (GES5-E, SEMILAB Sopra). Photocatalytic degradation of methylene blue (MB) (10<sup>−5</sup> M aqueous solution) using Si NWs was performed in a commercial photochemical reactor (Lelesil Innovative Systems, Mumbai). A time programmable visible lamp was used for illuminating the sample with excitation wavelength 390–730 nm. UV-vis absorption spectra were recorded in a Shimadzu 2450 UV-vis spectrophotometer.

**Table 1** Details of the growth conditions of MACE grown Si NWs and the sample codes

Si Wafer orientation	H <sub>2</sub> O <sub>2</sub> : HF (volume ratio)	Sample code
Si(100)	2 : 2	S1HF2
	2 : 3	S1HF3
	2 : 4	S1HF4
	2 : 5	S1HF5
	2 : 6	S1HF6
	2 : 7	S1HF7
	2 : 8	S1HF8
Si(111)	2 : 2	S2HF2
	2 : 3	S2HF3
	2 : 4	S2HF4
	2 : 5	S2HF5
	2 : 6	S2HF6
	2 : 7	S2HF7
	2 : 8	S2HF8

## 3. Results and discussions

### 3.1. Growth and morphology

MACE has been widely used for the growth of aligned Si NWs and the etching mechanism has been discussed by several groups.<sup>10,29,30,32,33,36,37</sup> It has been recognized that during the MACE process, under certain etching conditions mesoporous Si NWs are formed due to lateral etching and this gives rise to the formation of arbitrary shaped Si NCs on the surface of the Si NWs.<sup>10</sup> The shape and size of the Si NCs are decided by the size of the pores and intermediate distance between the pores. However, the morphologies of the as-etched Si wafers are

different for different etchant concentrations and the Si wafer orientations. Fig. 1 shows the FESEM cross sectional images of the samples of group S1 (1<sup>st</sup> row) and group S2 (2<sup>nd</sup> row). Fig. 2 shows the corresponding top-view FESEM images of the Si NWs. Note that the morphology of the NWs is different for two different orientation of the Si wafer *i.e.* Si(100) (group S1) and Si(111) (group S2). We discuss the growth process in group S1 first and then discuss it for the group S2. In case of Si(100), when the HF concentration is very small (2 : 2), the movement of Ag NPs are arbitrary on the Si wafer and porous Si is formed instead of Si NWs (Fig. 1(a) and 2(a)). With the increase in the HF concentration, the pores become more well defined and uniform and thus vertical NWs are formed (Fig. 1(b–e)). Note

that the NWs are slightly bent at the top portions and for higher concentration of HF (2 : 8) the Si NWs form bundles (Fig. 1(e) and 2(e)). However, interesting changes in growth direction and morphology have been observed in case of Si(111) wafer, when the H<sub>2</sub>O<sub>2</sub> : HF concentration ratio is systematically changed from 2 : 2 to 2 : 8. When the HF concentration is small (2 : 2), nearly straight but slightly slanted Si NWs are formed (Fig. 1(f)). With the increase of HF concentration, the NWs become slanted, kinked and zigzag directed. The mechanism behind different orientations of the NWs in two cases can be explained in the following way. According to the Si crystal structure, the (100) planes have two back bonds to the underneath atoms, while atoms on (111) planes have three back bonds.<sup>34</sup> The Si

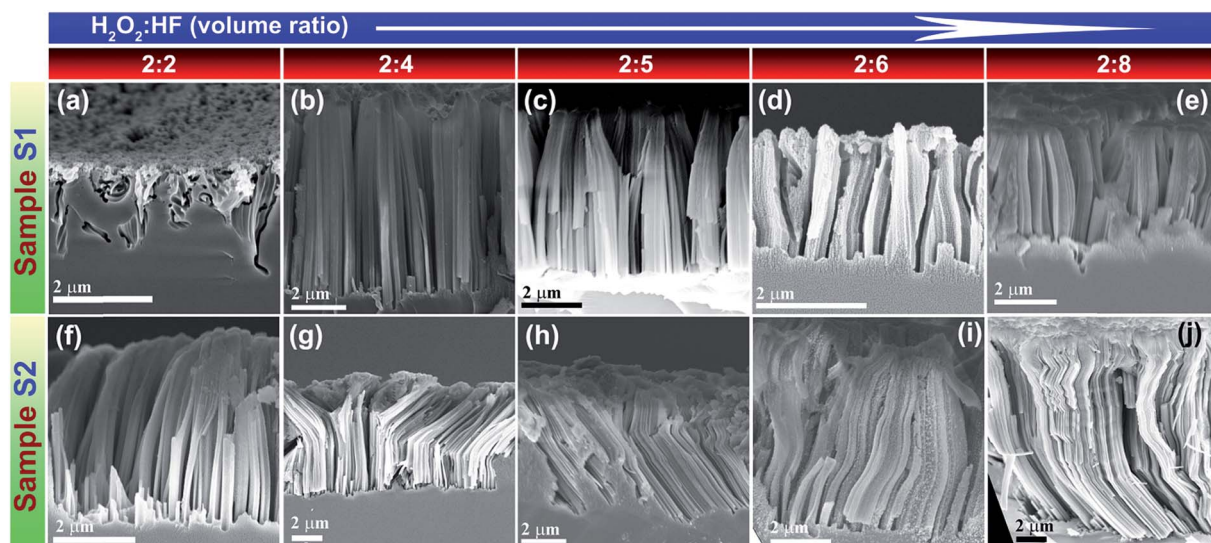


Fig. 1 Comparison of FESEM cross-sectional images of the group S1 ((a–e), 1<sup>st</sup> row) and group S2 ((f–j), 2<sup>nd</sup> row), for different concentrations of HF keeping the H<sub>2</sub>O<sub>2</sub> concentration fixed during the MACE process.

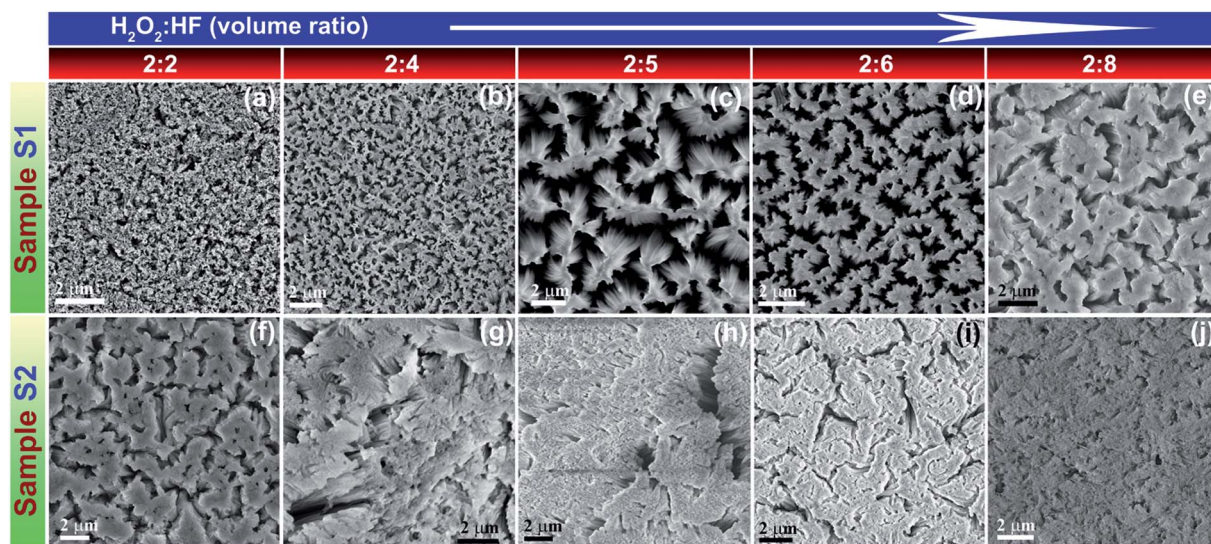


Fig. 2 Comparison of FESEM top-view images of surface morphology of the group S1 ((a–e), 1<sup>st</sup> row) and group S2 ((f–j), 2<sup>nd</sup> row), for different concentrations of HF keeping the H<sub>2</sub>O<sub>2</sub> concentration fixed during the MACE process.

atoms of (100) planes underneath the Ag NPs in HF/H<sub>2</sub>O<sub>2</sub> solution are easier to dissolve as compared with the Si atoms of (111) planes. As a result, the Si NWs are always vertical for Si(100) wafer as the etching takes place vertically ( $\langle 100 \rangle$  direction). In case of Si(111) wafer, the etching is highly anisotropic. When the HF concentration is low, the Si oxide formed on the etching front (underneath the Ag NPs) is not dissolved completely and the hole injection from oxidant to Si as well as dissolution of Si oxide is slower. As a result, etching happens on the preferable  $\langle 100 \rangle$  direction and the NWs are vertical for sample S2HF2. When the HF concentration is increased, the rate at which Si oxidation takes place is same as the dissolution rate. In this case, the anisotropic etching of Si occurs and kinked Si NWs are formed. When the HF concentration becomes sufficiently high, the dissolution of Si occurs rapidly and the NWs become zigzag.<sup>34</sup>

For the compositional analysis, we have performed EDX analysis on the Si NWs. Fig. 3(a) and (b) shows the EDX spectra measured on top surface of S1HF5 and S2HF5 confirming the presence of the Si and O on the Si NWs surfaces. The inset shows the corresponding elemental composition in atomic percentage. Fig. 3(c) and (d) depict the compositional color mapping of the surface of sample S1HF5 and S2HF5. The insets

in Fig. 3(c) and (d) show the color mapping of individual element "Si" (left corner), and "O" (right corner). The EDX analysis confirms that the Si NWs are covered with a thin layer of oxide layer which is highly oxygen deficient. Sample S1HF5 is covered with Si<sub>2</sub>O and sample S2HF5 is covered with SiO, as revealed from the compositional analysis. Thus, the oxygen content of the samples is quite different in two cases.

Several reports suggest that due to the mesoporous structure of the MACE grown Si NWs, arbitrary shaped Si NCs are formed on its surface.<sup>10,11</sup> Fig. 4(a) and (b) show the TEM images of a single Si NW taken from sample S1HF5 and S2HF5, respectively. The Si NW is straight for S1HF5, while it is zigzag in nature in case of S2HF5 and the angle in each corner of the zigzag NW is shown in Fig. 4(b). It is clear that the surface of the Si NW is rough due to the side wall etching and it gives rise to arbitrary shaped Si NCs on the surface of Si NWs. Fig. 4(b) confirms the zigzag Si NW with different growth direction as indicated in the figure. Fig. 4(c and d) shows the corresponding HRTEM images and Fig. 4(e and f) shows the corresponding SAED pattern of the Si NW/NCs. The orientations of the planes of the crystalline Si NWs/NCs are shown in Fig. 4(e) and (f). The roughness of the NW surface is indicated by the white dashed line, which confirms the presence of the Si NCs of arbitrary

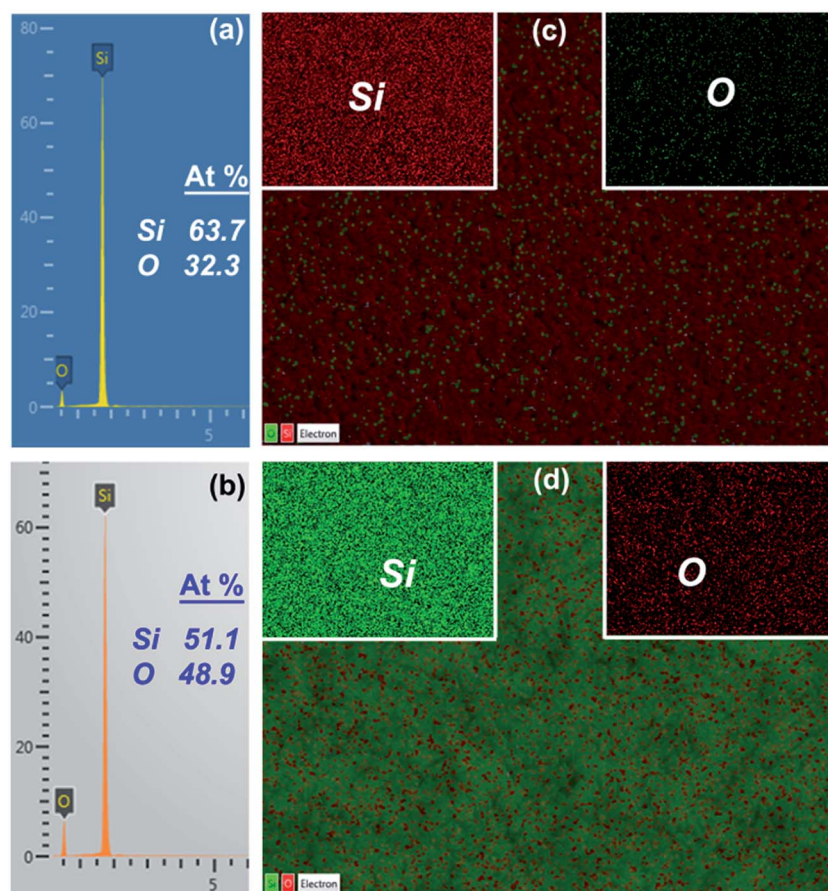


Fig. 3 EDX spectra of the samples: (a) S1HF5 and (b) S2HF5. The inset shows the corresponding elemental composition (in atomic percentage). The compositional color mappings of the surface of samples: (c) S1HF5 and (d) S2HF5. The insets of (c) and (d) show the color mapping of individual element Si (left corner) and O (right corner), respectively.

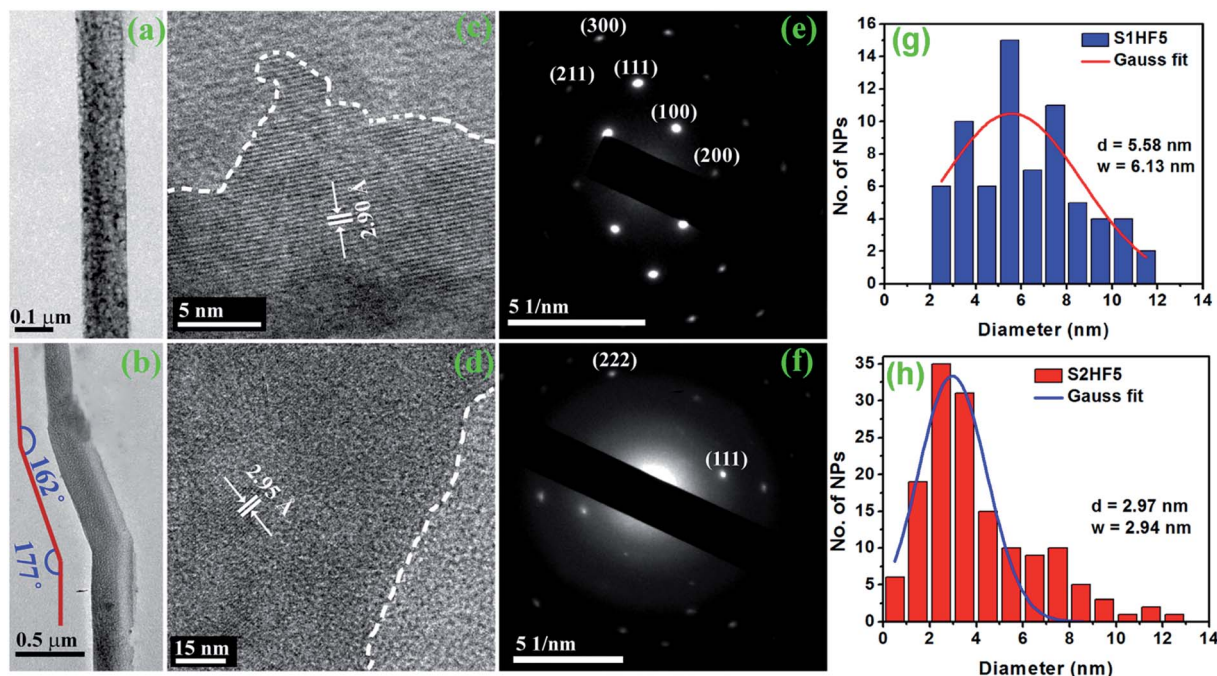


Fig. 4 TEM images of: (a) a straight Si NW in S1HF5 and (b) a zigzag Si NW in S2HF5. The growth direction of the Si NW in sample S2HF5 is indicated with corresponding angle in (b). (c and d) The corresponding HRTEM images showing the reduced lattice spacing (2.90 Å for sample S1HF5 and 2.95 Å for sample S2HF5). The presence of arbitrary shaped Si NCs on the surface of Si NW is indicated by a white dashed boundary. (e and f) The corresponding SAED pattern indicating the different orientations of the crystalline Si NWs/NCs. The size distribution of the Si NCs on the surface of the Si NWs for (g) S1HF5 and (h) S2HF5. The corresponding Gaussian fit (line) to the size distribution with the average diameter ( $d$ ) and FWHM ( $w$ ) is also shown for comparison.

shape (Fig. 4(c) and (d)). The lattice spacing  $d = 2.90$  Å in Fig. 4(c) and  $d = 2.95$  Å in Fig. 4(d) confirms that the Si NW/NCs are strained, single crystalline and (111) oriented. The reduced  $d$ -spacing (2.90 Å and 2.95 Å instead of 3.11 Å) implies a compressive strain in the lattice, which is related to the anisotropic etching and native oxide layer grown on the Si NW/NC surface.<sup>10</sup> The size distribution of Si NCs measured from sample S1HF5 and S2HF5 are shown in Fig. 4(g) and (h), respectively. The average diameter ( $d$ ) of the Si NCs is calculated by a Gaussian fit to the size distribution in Fig. 4(g) and (h) and the mean value of  $d$  in S1HF5 is  $\sim 5.58$  nm, while it is  $\sim 2.97$  nm in S2HF5. The full width at half maxima ( $w$ ) of the distribution is also high in case of sample S1HF5 (6.13 nm) as compared to the sample S2HF5 (2.94 nm). The evolution of mesoporous Si NWs has been discussed by several groups.<sup>30,32,33,38,39</sup> The difference in sizes of the Si NCs in two cases can be explained in the following way.  $\text{Ag}^+$  ions react with Si and extract electrons from  $\text{Ag}^+/\text{Si}$  surface and converts to Ag by creating pores on Si NWs surface and thus Si NCs are formed. Some reports suggest that crystal defects and impurities, such as dopant atoms in case of doped Si at the Si surface are thought to serve as nucleation sites for the pore formation.<sup>30,38</sup> Higher dopant concentration may create a larger thermodynamic driving force for pore formation, or at least increase the rate of etching and surface roughness. Similarly, higher dopant concentration lowers the energy barrier to charge injection across the Si surface. This results in higher porosity and hence the average size of the Si NCs decreases while its density increases.

Accordingly, we observed higher average diameter of Si NCs in S1HF5 ( $\sim 5.58$  nm) as compared to that of S2HF5 ( $\sim 2.97$  nm). Note that the concentration of HF in the etching solution also has a strong effect on the size and density of the Si NCs. The pre-deposited Ag NPs oxidized by  $\text{H}_2\text{O}_2$  becomes  $\text{Ag}^+$  in the close proximity of the Ag NPs. With the increase in HF concentration, relative concentration of  $\text{H}_2\text{O}_2$  decreases and hence the concentration of the  $\text{Ag}^+$  ions decreases. As a result, less fraction  $\text{Ag}^+$  ions nucleate at the defect sites and the density of pores decreases. Hence, the average size of the Si NCs increases and the Si NCs density decreases with increasing HF concentration.<sup>30,33,38,39</sup> Due to quantum confinement of the carriers in the Si NCs, these NCs strongly influence the photophysical properties of the MACE grown Si NWs.

### 3.2. XPS analysis

In order to investigate the atomic composition, surface states and the nature of defects, XPS studies were carried out on S1HF5 and S2HF5. XPS studies confirm that the Si NWs/NCs are covered by a native sub oxide layer of Si, *i.e.*,  $\text{SiO}_x$  ( $0 < x < 2$ ) layer. Fig. 5(a)–(c) shows the Si 2p core-level spectra of bulk Si, S1HF5 and S2HF5 respectively. Each curve is fitted with four Gaussian peaks after choosing appropriate baseline (Shirley). The peaks are assigned as peak 1, 2, 3 and 4. The fitted parameters are tabulated in Table 2. Fig. 5(d) shows the comparison of the core level O1s XPS spectra of the samples S1HF5 and S2HF5. Different peaks in Fig. 5(a)–(c) correspond to the neutral Si, its

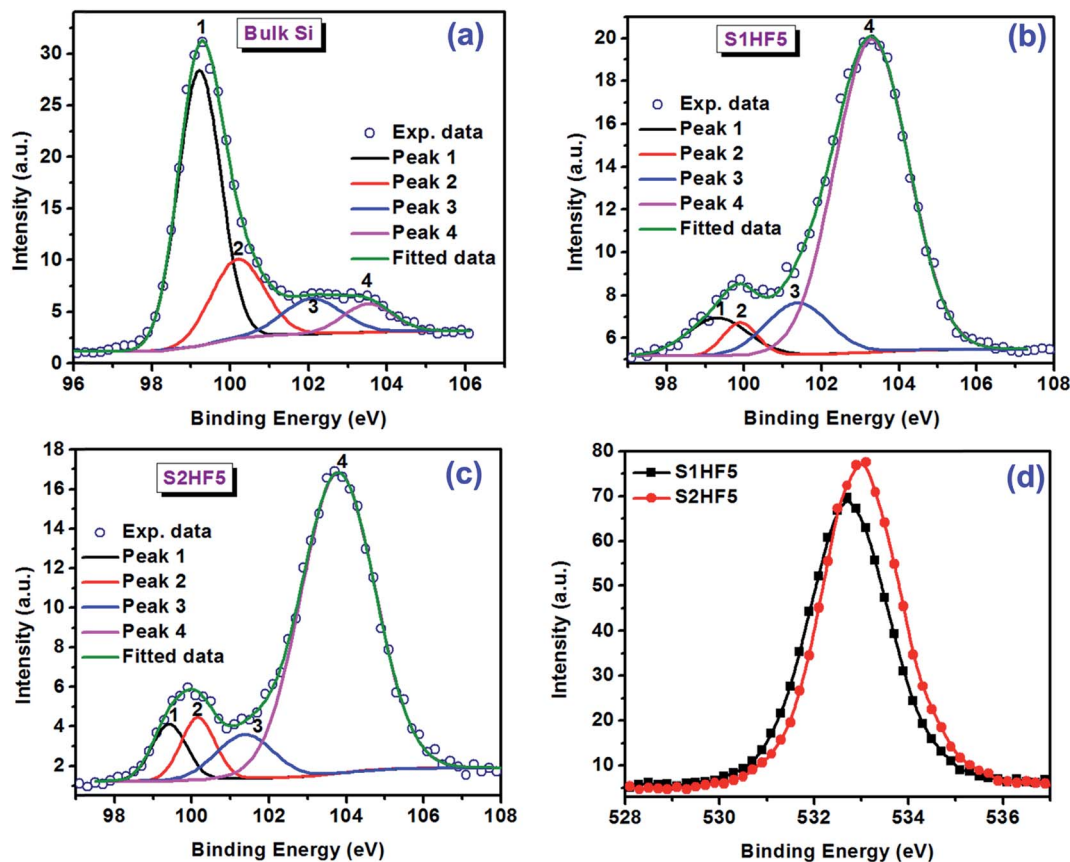


Fig. 5 Core level Si 2p XPS spectra of the samples: (a) bulk Si, (b) S1HF5, and (c) S2HF5. Each curve is fitted with four Gaussian peaks after subtracting appropriate baseline (Shirley). The peaks are labeled as peak 1, 2, 3 and 4. (d) Comparison of the core level O1s XPS spectra of the samples S1HF5 and S2HF5.

Table 2 The summary of the fitted peak parameters of Si 2p XPS core level spectra of samples S1HF5, S2HF5 and bulk Si

Sample	Peaks	Peak position (eV)	Peak identity
Bulk Si	Peak 1	99.2	Si <sup>0+</sup>
	Peak 2	100.2	Si <sup>1+</sup>
	Peak 3	102.1	Si <sup>2+</sup>
	Peak 4	103.5	Si <sup>3+</sup>
S1HF5	Peak 1	99.3	Si <sup>0+</sup>
	Peak 2	99.9	Si-H
	Peak 3	101.4	Si <sup>2+</sup>
	Peak 4	103.3	Si <sup>3+</sup>
S2HF5	Peak 1	99.4	Si <sup>0+</sup>
	Peak 2	100.1	Si-H
	Peak 3	101.4	Si <sup>2+</sup>
	Peak 4	103.8	Si <sup>3+</sup>

different oxidation states and the terminated surface states. The peak assignments made in Table 2 is consistent with the literature reports.<sup>35,40–42</sup> XPS analysis thus confirms the presence of SiO<sub>x</sub> layer on the Si NWs/NCs and this SiO<sub>x</sub> layer is responsible for the compressive strain in the Si NWs/NCs, as revealed from the HRTEM and the Raman analysis (discussed later). The O1s peak from SiO<sub>2</sub> has a reported binding energy of 533.6 eV.<sup>41</sup> From the O1s spectrum in Fig. 5(d), the XPS peak at ~532.7 eV

in S1HF5 and ~533.0 eV in S2HF5 are attributed to O<sup>-</sup> ions in the Si-O bonds due to the sub-oxide layer of Si, which is consistent with the Si 2p core level spectrum.<sup>43,44</sup> From the XPS compositional analysis, the atomic ratio of oxygen to Si is found to be ~1.80 for S1HF5 and ~1.85 for S2HF5. This leads to the nonbridging oxygen hole center (NBOHC, ≡Si-O\*, where, “\*” represents an unpaired hole) defects in the SiO<sub>x</sub> layer. This is confirmed from the defect related PL emission from these samples (discussed later).

### 3.3. Raman analysis

In order to assess the crystallinity/amorphicity, presence of H-terminated surface and the dimension of Si NCs on the Si NWs surface, micro-Raman measurements were carried out using 514 nm laser excitation.<sup>11</sup> Fig. 6(a) and (b) depict a comparison of the 1<sup>st</sup> order Raman spectra of group S1 and S2 etched with different concentration of HF. The Raman spectra of different sample were compared by taking the first order Raman peak of the bulk Si at 520.5 cm<sup>-1</sup> as reference (dotted vertical line). Fig. 6(c) and (d) depict a comparison of the corresponding 2TO Raman mode of the same group of samples (S1 and S2). The inset in Fig. 6(c) and (d) show the enlarged view of a portion of the Raman spectra in the range 2000–2350 cm<sup>-1</sup> to ascertain the presence of Si-H bonds in the respective samples.

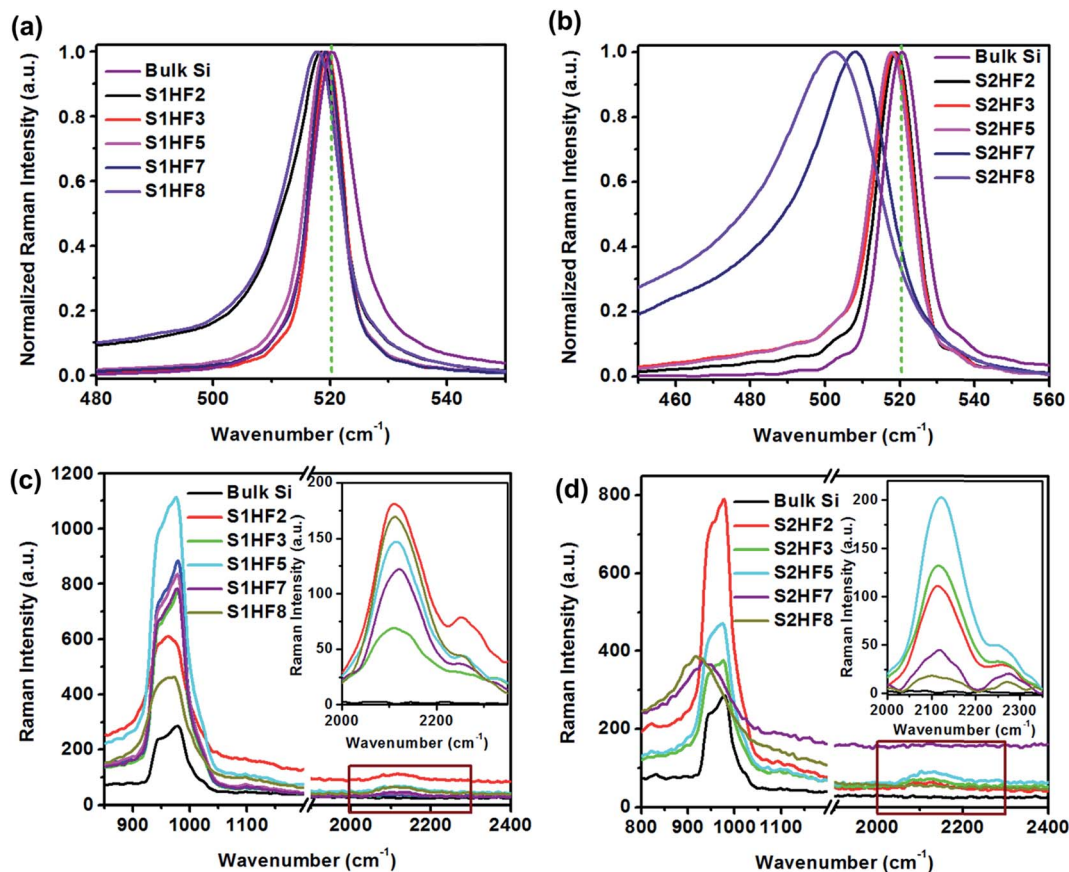


Fig. 6 Comparison of the 1<sup>st</sup> order Raman spectra for the Si NWs grown with different concentrations of HF: (a) S1 and (b) S2 groups. The spectra are normalized to assess the peak shift from the bulk Si 1<sup>st</sup> order Raman peak at 520.5 cm<sup>-1</sup> (indicated by dotted vertical line). (c and d) Comparison of the Raman spectra showing the 2<sup>nd</sup> order Raman mode (2TO) for samples in S1 and S2 with that of the bulk Si. The inset in (c) and (d) shows the enlarged view of the range 2000–2350 cm<sup>-1</sup> to ascertain the presence of Si–H bonds in the respective samples.

Note that the 1<sup>st</sup> order Raman spectrum of each sample shows a red shift and asymmetry in the lower energy range. These Raman shifts ( $\Delta\omega$ ) and asymmetry can be explained based on the competing effect of phonon confinement and strain on the Si NWs/NCs.<sup>10,11,45–47</sup> The  $\Delta\omega$  is positive (blue shift) for compressive strain and negative (red shift) for tensile strain.<sup>10,11,47</sup> Since the red-shift in S1 group is very small compared to the shift expected from the phonon confinement effect due to the ultra-small Si NCs,<sup>11</sup> the blue shift expected from the compressive strain due to the SiO<sub>x</sub> layer may be partly compensated by the red-shift expected from the size effect. However, the samples S2HF7 and S2HF8 show completely different features in Fig. 6(b) and (d). In this case, the TO and 2TO Raman modes are deformed and the shift is beyond the phonon confinement limit. It implies that the Si NWs top surface become amorphous in nature. Note that the tail of the 1<sup>st</sup> order Raman peak is extended down to 460 nm (Fig. 6(b)), which falls in the region TO Raman mode of amorphous Si (480 cm<sup>-1</sup>). The 1<sup>st</sup> order Raman peak of S1HF7 and S1HF8 (Fig. 6(a)) show features similar to those of samples in group S2 though the peak shift is less in former case as compared to the latter case. Higher concentration of HF creates higher fraction of amorphous regions in the MACE grown Si NWs. Interestingly,

the Raman data shown in the insets of Fig. 6(c) and (d) confirms that the stretching modes of Si–H bonds are present in each Si NWs/NCs grown by MACE.<sup>48</sup> The Si–H bonds play a crucial role in the photocatalytic process (discussed later).

### 3.4. Visible-NIR PL

Si NWs fabricated by MACE method usually exhibit broad band PL in the visible-NIR region at RT.<sup>10,30,31,49,50</sup> Fig. 7(a) and (b) show a comparison of the visible PL spectra of the samples in group S1 and S2, respectively, grown using different concentration of HF during MACE process. Each sample show strong visible PL band covering the range 1.4–2.4 eV. Due to large diameter and indirect bandgap of the Si NWs, the strong visible PL is unlikely to originate from the Si NWs core. On the other hand, the dimensions of the self-grown Si NCs (as shown in Fig. 4(g and h)) with a broad distribution in sizes which are comparable/smaller than the excitonic Bohr diameter (~10 nm) in Si. Therefore, the QC effect of carriers in the Si NCs, instead of that in Si NWs, is most likely responsible for the visible PL shown in Fig. 7(a) and (b).<sup>10</sup> In our previous studies, we have quantitatively analyzed the PL spectra of Si NCs decorated Si NWs and argued that the visible PL is primarily contributed by

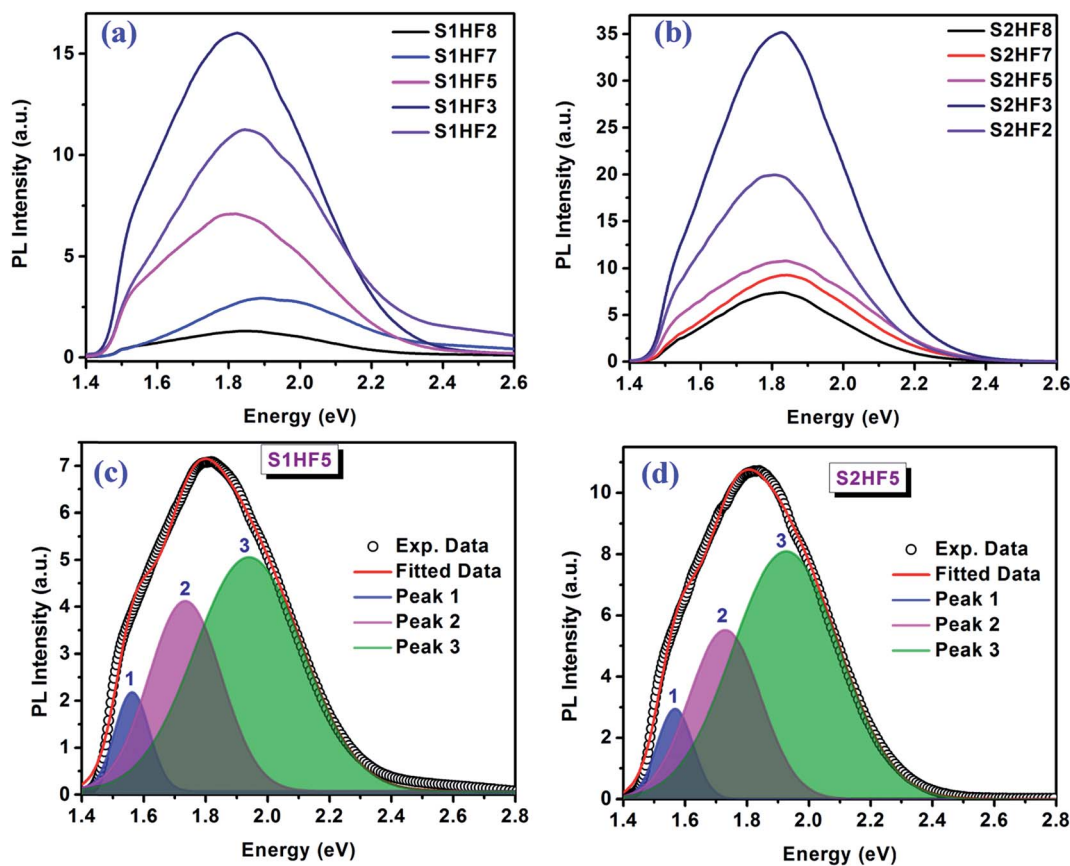


Fig. 7 Comparison of the RT PL spectra of the Si NWs grown at different concentrations of HF for group: (a) S1 and (b) S2. PL spectra fitted with Gaussian peaks for samples: (c) S1HF5 and (d) S2HF5.

the Si NCs due to QC effect.<sup>10,11</sup> However, it is clear from XPS and EDX that in the present case the Si NWs are covered with oxygen deficient  $\text{SiO}_x$  layer. The NBOHC defects within  $\text{SiO}_x$  matrix in core-shell Si/ $\text{SiO}_x$  nanostructure also contribute to the observed visible PL.<sup>22–24</sup> In order to clarify its contribution, we have fitted each spectrum with three Gaussian bands. Fig. 7(c) and (d) show the fitted PL spectra of the sample S1HF5 and S2HF5, respectively. The low intensity peak 1 is an artifact of the measurement arising from the incident laser (2<sup>nd</sup> harmonic of 405 nm, *i.e.*, 810 nm). Peak 2 is attributed to the QC effect in the Si NCs embedded in  $\text{SiO}_x$  matrix.<sup>10,11,15,49</sup> The deep red PL at  $\sim 1.93$  eV (peak 3) is attributed to the NBOHC defects in the  $\text{SiO}_x$  layer.<sup>22–24</sup> It may be noted that PL spectral position and intensity in each case depend on the doping type and doping density of the initial Si wafers. It is clear from Fig. 7(a and b) that the PL intensity of the samples depends on the HF concentration during the growth. Fig. S11 (ESI<sup>†</sup>) shows the comparison of the integrated PL intensity of samples in group S1 and S2 as a function of HF concentration. It is clear that the integrated PL intensity of each sample in group S2 is higher than that of the corresponding samples in group S1. Since the S2 samples have higher density of Si NCs than that of S1, the corresponding PL intensities are higher in S2 than those in S1. This is consistent with our earlier reports.<sup>11,19</sup> A nonmonotonic change in PL intensity with HF concentration can be understood from the following competing effects: at lower HF concentration, the dissolving rate of Si oxide

formed at the etching front is slow. Owing to the undissolved Si oxide, the NBOHC defect density is higher at lower concentration of HF. As a result, the PL intensities would be higher for the samples grown using lower HF concentration.<sup>19</sup> However, at very low concentration of HF (2 mL and 3 mL HF for group S1), the formation of Si NWs is incomplete and only a porous-like Si surface is formed. Due to incomplete NW formation, the lateral etching is also very less and thus the density of Si NCs are very low. This gives rise to the lower intensity of PL. It has been pointed out in our earlier report that the PL intensity increases with increase in the length of the Si NWs due to the higher density of Si NCs and NBOHC defects.<sup>11,19</sup> When the density of the NCs and the NBOHC defects are significant, the resulting PL intensity attains a maximum. At higher HF concentration, NBOHC defects decreases and as a result the resultant PL intensity decreases. Thus, the integrated PL intensity shows a maximum for a certain concentration of HF in S1 and S2 group of samples. Note that at very high HF concentration (2 : 7 and 2 : 8), the top portions of the Si NW layer becomes amorphous in nature that may be partly responsible for the low intensity PL of the respective samples.

### 3.5. Optical reflectivity

In order to better understand the relative intensity of PL and photocatalytic nature (discussed later) of different samples,

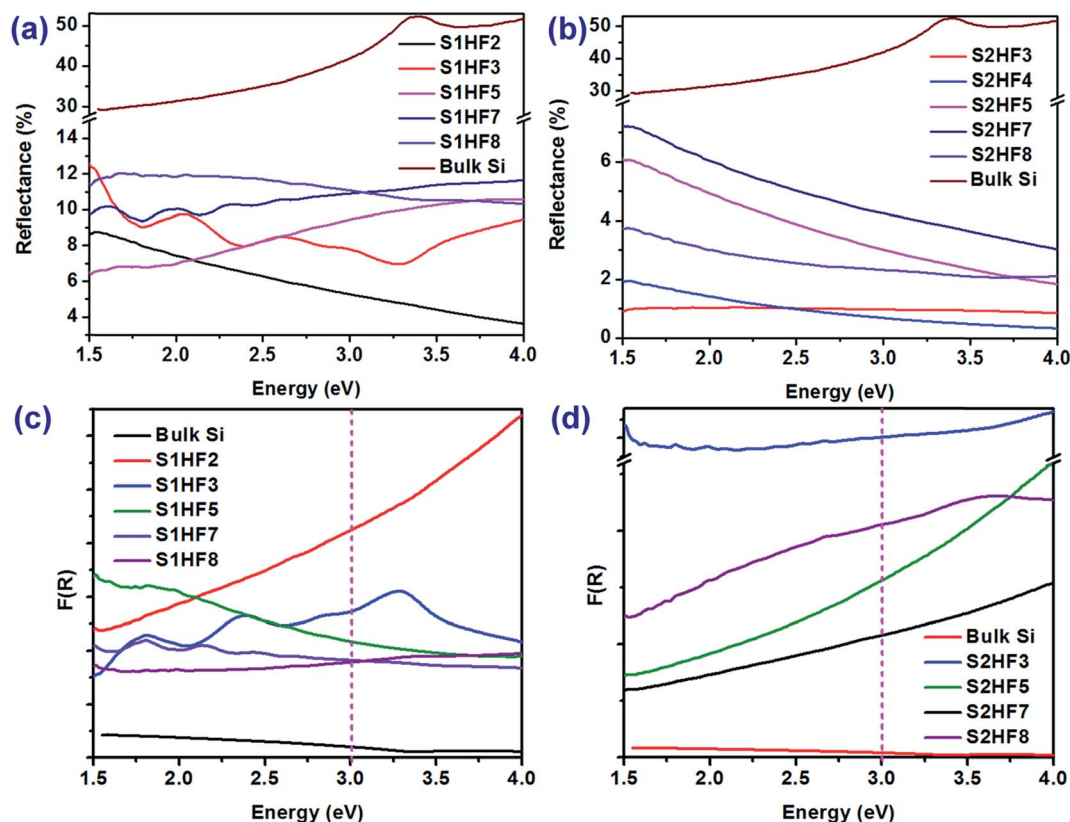


Fig. 8 Comparison of the diffused reflectance spectra for samples etched with different HF concentrations for group: (a) S1 and (b) S2. (c) and (d) The corresponding Kubelka–Monk absorption function  $F(R)$  for S1 and S2. The vertical dashed line indicates the value of  $F(R)$  at 3.06 eV (laser excitation for PL).

diffused reflectivity was measured for the Si NWs/NC samples under oblique incidence (P-polarized light). Fig. 8(a) shows comparison of the diffused reflectivity as a function of energy for the bulk Si wafer and samples in group S1 grown for different HF concentration. Fig. 8(b) shows the same for samples in group S2. Absorption coefficient of the Si NWs/NCs was assessed by using the Kubelka–Monk function  $F(R)$ . Fig. 8(c) and (d) show the plot of  $F(R)$  as a function of energy for different samples in group S1 and S2, respectively. Due to multiple reflections on the inner surface of the Si NWs and a broad range of size distribution of the Si NCs, the absorption is significantly high in case of Si NWs/NCs over the entire range of wavelength. Thus, higher PL intensity is partly caused by the higher absorption of the samples, as shown by the vertical dashed line in Fig. 8(c) and (d). The residual Ag NPs lying at the lower part and partly at the surface of the NWs may cause higher absorption in the visible range due to the surface plasmon resonance effect.<sup>31</sup> Since the NWs were etched in  $\text{HNO}_3$  solution after growth, its contribution is expected to be less. However, lower reflectivity implies higher absorption and more efficient excitation of carriers, which could lead to the enhanced radiative recombination and/or efficient charge separation. Ultra low reflectivity of the Si NWs is extremely beneficial for high efficiency solar photovoltaic and photocatalytic applications.

### 3.6. Visible light photocatalysis

The excitons generated within the NC decorated Si NWs could be energetic enough to drive applicable photoelectrochemical reactions due to its wide range of optical absorption with high intensity and broad visible emission centered near the red-infrared region. Fig. 9(a) and (b) show the comparison of the visible light photodegradation of methylene blue (MB) in presence of Si NWs grown by using different concentration of HF. The photographs of the change in MB color due to the photodegradation at an interval 20 min for S1HF8 and S2HF8 are shown in Fig. 9(C1) and (C2), respectively. In each case, a small piece (area  $\sim 1.5 \text{ cm}^2$ ) of Si NWs sample was kept in a beaker containing 100 mL of MB solution and it was exposed to visible light (390–730 nm) for different durations with a programmable Xe lamp (250 W). When a photon with energy equal to or greater than the band gap of the Si NWs/NCs reaches the catalyst's surface, it results in the generation of an electron in the conduction band and a hole in the valence band. The induced hole receives the electron from adsorbed water and results in  $\cdot\text{OH}$  free radical groups.<sup>25,26</sup> XPS and Raman spectra confirm that the Si–H bonds are present on the Si NCs/NWs and XPS spectra along with PL analysis confirm that the  $\text{SiO}_x$  over layer are NBOHC defected. The electron deficient Si–H surface states present in the samples serve as an electron sink and hence accelerate the separation of photoinduced e–h pairs, which

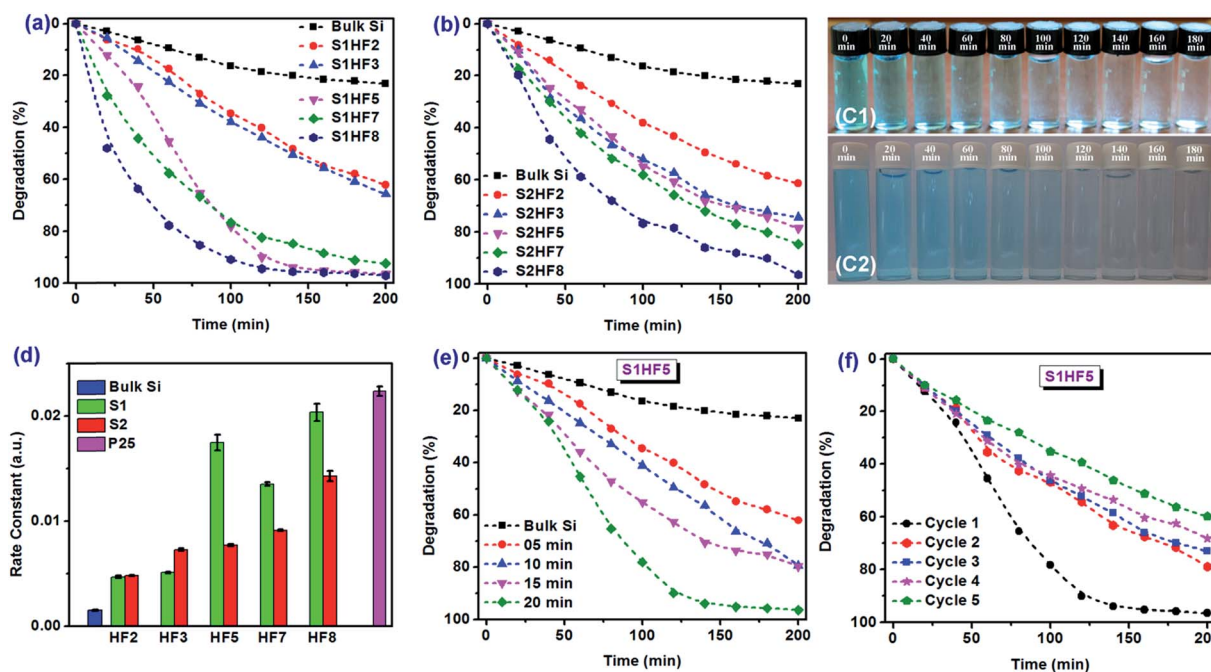


Fig. 9 Comparison of the visible light photodegradation of MB in presence of Si NWs/NCs for group: (a) S1 and (b) S2. The photographs of the change in color of MB color due to the photodegradation with Si NWs/NCs taken after every 20 min for (C1) S1HF8 and (C2) S2HF8. (d) Comparison of the photodegradation rate constant for S1 and S2 at different HF concentration. The rate constant of standard P25 measured in MB solution is also shown for comparison. (e) Comparison of the photodegradation of MB in presence of sample S1HF5 grown for different etching time (5, 10, 15 and 20 min). (f) Comparison of the photodegradation of MB of sample S1HF5 for different cycle.

endorses the photocatalytic activity of the Si NWs/NCs. Finally, the reactive  $\cdot\text{OH}$  radicals oxidize and degrade the MB by destructing the chain of the organic molecule.<sup>25,26</sup> It has been reported that H-terminated Si NCs covered by Si sub-oxide is possibly the best Si based photocatalyst compared to the other Si structure (bulk Si and Si nanostructure). However, in the present case, in both type of samples S1 and S2, the photocatalytic efficiency increases with the increase in HF concentration during etching. Higher concentration of HF causes higher density of Si-H bonds and it results in higher degradation efficiency. Analysis of the data shows that the degradation of MB in the present case follows the 1<sup>st</sup> order degradation kinetics in presence of the MACE grown Si NWs/NCs. We have calculated the degradation rate constant ( $k$ ) for each sample in groups S1 and S2 and the results are shown in Fig. 9(d). We have compared the photocatalytic efficiency of the MACE grown Si NWs sample with that of the industry standard photocatalyst<sup>51</sup> P25 ( $\text{TiO}_2$ ) and the corresponding rate constant is shown in Fig. 9(d). The rate constant  $k$  was obtained by fitting the concentration data to the rate equation:  $\ln(C_t/C_0) = -kt$ , where  $k$  is apparent rate constant,  $C_t$  is the actual concentration at time  $t$ , and  $C_0$  the initial concentration of MB. The data in Fig. 9(a and b) follows the above equation with a good fit for different samples, thus confirming the first-order rate kinetics. A plot of  $\ln(C_t/C_0)$  vs. light exposure time for each sample and its linear fit is shown in Fig. S12 (ESI<sup>†</sup>). Interestingly, it is found that MACE grown Si NWs performance is quite comparable to that of commercial P25 samples. In this case, a thin film of P25 was prepared by immersing a  $1.5 \text{ cm}^2$  Si wafer (same as that of Si

NWs samples) in to a  $20 \text{ mg L}^{-1}$  aqueous solution of P25. The value of  $k$  is  $0.020 \text{ min}^{-1}$  for the sample S1HF8, while it is  $0.022 \text{ min}^{-1}$  for P25. Earlier report suggests that the visible light photocatalytic rate constant of P25 in MB solution is  $0.0076 \text{ min}^{-1}$  which is very low compared to our results.<sup>52</sup> Note that in our case the light source wavelength is in the range 390–730 nm, while it was 420–800 nm in the above reported case. Due to presence of some near UV wavelengths, the rate constant is higher in the present study with P25. However, it is clear from Fig. 9(d) that the value of  $k$  is higher for higher HF concentration etching case due to the stronger presence of H-terminated surface. The increase in  $k$  value is higher for S1 group as compared to the S2 group samples. At higher HF concentration, the amorphous Si fraction in group S2 is higher (as evidenced by the Raman spectra of Fig. 6(b and d)) that partly prevents the formation of H-terminated surface, and thus the degradation rate is less in group S2 as compared to those of group S1. Thus, the samples in S1 show the higher value of  $k$  as compared to the samples in S2. Note that the photocatalytic activity of the Si NWs/NCs samples strongly depends on the surface area of the Si NWs/NCs in contact with the MB solution. The length of the Si NWs varies almost linearly with the etching (MACE) duration and we have checked the photocatalytic efficiency of the Si NWs grown for different etching duration keeping the etchant concentration unaltered.<sup>36</sup> Fig. 9(e) shows the comparison of the photodegradation efficiency of sample S1HF5 grown for different etching duration (5, 10, 15 and 20 min). Higher etching duration causes higher length of the NWs, higher surface area and higher density of Si NCs, which result in

enhanced absorption and creation of more e–h pairs finally leading to the higher photodegradation efficiency.<sup>10,11</sup> Note that the Ag nanoparticles (NPs) could not be fully removed from the pores of the Si NWs after HNO<sub>3</sub> etching.<sup>19</sup> The residual Ag NPs present within pores between the Si NWs and on the surface of the Si NCs may contribute to the enhanced photocatalytic activity of the Si NWs/NCs. Because of the differences in their Fermi levels, it can introduce a Schottky barrier between the Ag NPs and Si NWs/NCs. The built-in potential at the Schottky diode junction can facilitate the efficient separation of photo-generated e–h pairs and influences the degradation of MB.<sup>19</sup>

In order to evaluate the stability and recyclability of the photocatalyst (MACE grown Si NWs), the photodegradation of MB was repeated for multiple cycles. Fig. 9(f) shows the comparison of photodegradation of MB in S1HF5. After each cycle, the sample is taken out and rinsed in DI water. It is well known that immersion of Si NWs in diluted HF solution results in partial removal of the oxide layer. However, HF treatment can also create H-terminated Si surface, which can take active part in MB degradation.<sup>53</sup> In order to avoid H-terminated surface, we have recovered the sample after each cycle by cleaning it with DI water only. It is clear from Fig. 9(f) that 96.5% MB is degraded in first cycle and 59.8% after 5<sup>th</sup> cycle. This is because of the formation of Si oxide and elimination of Si–H surface states. However, HF treatment can partly recover the stability.<sup>53</sup>

It is interesting to note that the MACE grown samples show highly efficient PL as well as impressive photocatalytic efficiency under the visible light illumination. Earlier reports suggest that two such contrastive phenomena can be simultaneously present in a single system.<sup>19,54</sup> The PL process requires a fast radiative recombination of the excited e–h pairs, while the photocatalysis requires an easy separation of the photoexcited e–h pairs with minimum recombination. Thus, if the former process is dominant, the later process will be less effective. It has been reported that the H-terminated surface is mostly responsible

for the excellent photocatalytic activity of the MACE grown Si NWs,<sup>19,25,27</sup> while the QC effect in Si NCs and the NBOHC defects are mainly responsible for the efficient PL.<sup>10,19,23,24</sup> We have found that the MACE grown Si NWs/NCs with higher concentration of HF etching shows highly efficient photodegradation (Fig. 9(a and b)) and less efficient PL (Fig. 7(a and b)) as compared to that grown with lower concentration of HF. As expected we indeed found that the efficiencies of the above two processes are complementary to each other in different samples. Fig. 10(a) shows the variation of integrated PL intensity of the samples in group S2 as a function of relative HF concentration, while Fig. 10(b) shows the photodegradation efficiency of the corresponding samples. It is clear from Fig. 10 that as the HF concentration increases, the integrated PL intensity decreases, while the photodegradation efficiency systematically increases. As mentioned earlier, higher HF concentration causes higher density of Si–H bonds which results in higher photodegradation efficiency, while lower HF concentration causes higher Si NCs density and higher density of NBOHC defect sites which results in the PL intensity enhancement. Thus, depending on the requirement, one can tune the etchant concentration in the MACE process to suit one's need. Our results show that straight Si(100) NWs grown in case of S1 show superior photocatalytic activity as compared to that of zigzag Si(111) NWs grown in S2. The corresponding PL intensity is lower in S1 than that of S2. Though the resistivity of the starting wafers is different in two cases, the higher photocatalytic activity in S1 is believed to be due to the superior charge transport across the straight NWs as compared to the zigzag NWs in S2. Note that sample S2 has lower resistivity than S1, which yields higher density of NCs and NBPNC defects giving rise to higher intensity of PL. It may be noted that at low HF concentration, the NWs are straight in both cases and they have comparable photocatalytic efficiency (see Fig. 9(d)). Thus, straight NWs are preferable for photocatalytic applications, while zigzag NWs may be useful for light trapping and light emitting applications. Further experiments with wafers of same resistivity but different orientations are needed to elaborate on this issue. Our results demonstrate the supremacy of MACE process for the progress of Si NWs and open up the possibility of using the MACE grown Si NWs array for various light emitting and visible light photocatalytic applications.

## 4. Conclusions

We have demonstrated orientation controlled growth of Si NWs by simple MACE of Si wafers using Ag as the noble metal catalyst and HF/H<sub>2</sub>O<sub>2</sub> as the etchant. We have achieved straight, bent, kinked and zigzag Si NWs by choosing appropriate orientation of the starting Si wafer and concentration of etching solution. High resolution FESEM and TEM imaging confirmed that the Si NWs are decorated with ultra-small size arbitrary shaped Si nanocrystals (NCs) due to the lateral etching of the NWs. A strong broad band visible to NIR PL in the range 1.4–2.4 eV is observed from these Si NWs/NCs at RT and it is concluded that the QC of carriers in Si NCs and the NBOHC defect in the SiO<sub>x</sub> layer both contribute to the visible-NIR PL. In addition to

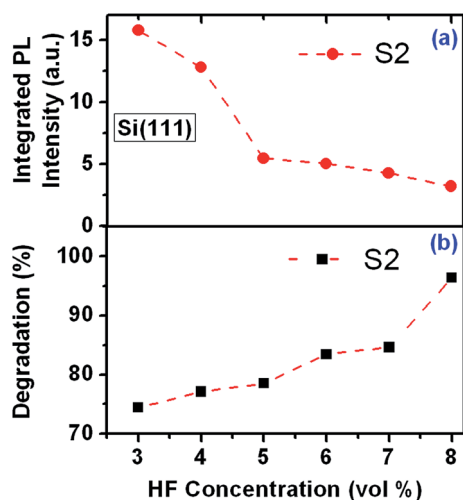


Fig. 10 (a) Integrated PL intensity and (b) photodegradation of MB as a function of HF concentration keeping the H<sub>2</sub>O<sub>2</sub> concentration fixed for Si(111) samples. The symbol in each case refers to the experimental data points, while the dashed line is a guide to the eye.

the efficient PL emission, the MACE grown Si NWs are shown to be excellent photocatalyst with visible light for the degradation of MB and the photocatalytic effect is quite stable up to 5 cycles of visible light illumination. The Si-H bonds present on the surface of the Si NWs/NCs facilitate the photocatalytic activity by efficient the separation of photogenerated e-h pairs. At higher HF concentration of etching, the density of NBOHC defects decreases resulting in lower PL intensity, while the density of Si-H bonds increases resulting in higher photocatalytic efficiency. Our interpretations are strongly supported by the HRTEM, EDX, Raman and XPS analyses. Our results open up possibility of using Si NWs array in white light LED as well as organic waste treatment and hydrogen production by photocatalytic water splitting.

## Acknowledgements

We acknowledge the financial support from CSIR (Grant No. 03(1270)/13/EMR-II), DEITY (Grant No. 5(9)/2012-NANO(VOL-II)) and BRNS (Grant No. 2012/37P/1/BRNS) for carrying out part of this work. Central Instruments Facility, I.I.T. Guwahati is acknowledged for the TEM, FESEM and micro-Raman facilities. We thank Dr K. Imakita, Kobe University for help in the XPS measurement.

## References

- 1 H. Savin, P. Repo, G. von Gastrow, P. Ortega, E. Calle, M. Garin and R. Alcubilla, *Nat. Nanotechnol.*, 2015, **10**, 624.
- 2 R. Yan, D. Gargas and P. Yang, *Nat. Photonics*, 2009, **3**, 569.
- 3 K. W. Lim, J.-I. Lee, J. Yang, Y.-K. Kim, H. Y. Jeong, S. Park and H. S. Shin, *ACS Appl. Mater. Interfaces*, 2014, **6**, 6340.
- 4 S. Su, X. Wei, Y. Zhong, Y. Guo, Y. Su, Q. Huang, S.-T. Lee, C. Fan and Y. He, *ACS Nano*, 2012, **6**, 2582.
- 5 D. Liu, L. Li, Y. Gao, C. Wang, J. Jiang and Y. Xiong, *Angew. Chem., Int. Ed.*, 2015, **54**, 2980.
- 6 H.-C. Chen, Y.-T. Chen, R.-Y. Tsai, M.-C. Chen, S.-L. Chen, M.-C. Xiao, C.-L. Chen and M.-Y. Hua, *Biosens. Bioelectron.*, 2015, **66**, 198.
- 7 R. Ghosh and P. K. Giri, *Sci. Adv. Today*, 2016, **2**, 25230.
- 8 J. Valenta, B. Bruhn and J. Linnros, *Nano Lett.*, 2011, **11**, 3003.
- 9 R. Ghosh, P. K. Giri, K. Imakita and M. Fujii, *J. Alloys Compd.*, 2015, **638**, 419.
- 10 R. Ghosh, P. K. Giri, K. Imakita and M. Fujii, *Nanotechnology*, 2014, **25**, 045703.
- 11 R. Ghosh, A. Pal and P. K. Giri, *J. Raman Spectrosc.*, 2015, **46**, 624.
- 12 M. V. Wolkin, J. Jorne, P. M. Fauchet, G. Allan and C. Delerue, *Phys. Rev. Lett.*, 1999, **82**, 197.
- 13 L. E. Brus, P. F. Szajowski, W. L. Wilson, T. D. Harris, S. Schuppler and P. H. Citrin, *J. Am. Chem. Soc.*, 1995, **117**, 2915.
- 14 M. Ehbrecht, B. Kohn, F. Huisken, M. A. Laguna and V. Paillard, *Phys. Rev. B: Condens. Matter Mater. Phys.*, 1997, **56**, 6958.
- 15 G. Ledoux, J. Gong, F. Huisken, O. Guillois and C. Reynaud, *Appl. Phys. Lett.*, 2002, **80**, 4834.
- 16 T. Matsumoto, J. I. Suzuki, M. Ohnuma, Y. Kanemitsu and Y. Masumoto, *Phys. Rev. B: Condens. Matter Mater. Phys.*, 2001, **63**, 195322.
- 17 O. Demichel, V. Calvo, P. Noé, B. Salem, P. F. Fazzini, N. Pauc, F. Oehler, P. Gentile and N. Magnea, *Phys. Rev. B: Condens. Matter Mater. Phys.*, 2011, **83**, 245443.
- 18 K. Kusova, L. OndiC, E. Klimesova, K. Herynkova, I. Pelant, S. Danis, J. Valenta, M. Gallart, M. Ziegler, B. Honerlage and P. Gilliot, *Appl. Phys. Lett.*, 2012, **101**, 143101.
- 19 R. Ghosh, K. Imakita, M. Fujii and P. K. Giri, *Phys. Chem. Chem. Phys.*, 2016, **18**, 7715.
- 20 L. T. Canham, *Appl. Phys. Lett.*, 1990, **57**, 1046.
- 21 A. R. Guichard, R. D. Kekatpure, M. L. Brongersma and T. I. Kamins, *Phys. Rev. B: Condens. Matter Mater. Phys.*, 2008, **78**, 235422.
- 22 S. S. Walavalkar, C. E. Hofmann, A. P. Homyk, M. D. Henry, H. A. Atwater and A. Scherer, *Nano Lett.*, 2010, **10**, 4423.
- 23 T. Suzuki, L. Skuja, K. Kajihara, M. Hirano, T. Kamiya and H. Hosono, *Phys. Rev. Lett.*, 2003, **90**, 186404.
- 24 L. Skuja, T. Suzuki and K. Tanimura, *Phys. Rev. B: Condens. Matter Mater. Phys.*, 1995, **52**, 15208.
- 25 M. Shao, L. Cheng, X. Zhang, D. D. D. Ma and S. T. Lee, *J. Am. Chem. Soc.*, 2009, **131**, 17738.
- 26 Y. Qu, X. Zhong, Y. Li, L. Liao, Y. Huangbc and X. Duan, *J. Mater. Chem.*, 2010, **20**, 3590.
- 27 N. Megouda, Y. Cofinier, S. Szunerits, T. Hadjersi, O. ElKechai and R. Boukherroub, *Chem. Commun.*, 2011, **47**, 991.
- 28 Z. Kang, C. H. A. Tsang, N. B. Wong, Z. Zhang and S.-T. Lee, *J. Am. Chem. Soc.*, 2007, **129**, 12090.
- 29 K. Q. Peng, Y. J. Yan, S. P. Gao and J. Zhu, *Adv. Mater.*, 2002, **14**, 1164.
- 30 Y. Qu, H. Zhoua and X. Duan, *Nanoscale*, 2011, **3**, 4060.
- 31 W. Chern, K. Hsu, I. S. Chun, B. P. d. Azeredo, N. Ahmed, K. H. Kim, J.-m. Zuo, N. Fang, P. Ferreira and X. Li, *Nano Lett.*, 2010, **10**, 1582.
- 32 C.-Y. Chen and C.-P. Wong, *Nanoscale*, 2015, **7**, 1216.
- 33 Z. Huang, N. Geyer, P. Werner, J. de Boor and U. Gosele, *Adv. Mater.*, 2011, **23**, 285.
- 34 Z. Huang, T. Shimizu, S. Senz, Z. Zhang, N. Geyer and U. Gösele, *J. Phys. Chem. C*, 2010, **114**, 10683.
- 35 E. G. Barbagiovanni, L. V. Goncharova and P. J. Simpson, *Phys. Rev. B: Condens. Matter Mater. Phys.*, 2011, **83**, 035112.
- 36 A. Pal, R. Ghosh and P. K. Giri, *Appl. Phys. Lett.*, 2015, **107**, 072104.
- 37 V. Kumar, S. K. Saxena, V. Kaushik, K. Saxena, A. K. Shukla and R. Kumar, *RSC Adv.*, 2014, **4**, 57799.
- 38 A. I. Hochbaum, D. Gargas, Y. J. Hwang and P. Yang, *Nano Lett.*, 2009, **9**, 3550.
- 39 J. Kim, H. Han, Y. H. Kim, S. H. Choi, J. C. Kim and W. Lee, *ACS Nano*, 2011, **5**, 3222.
- 40 S. Kim, M. C. Kim, S. H. Choi, K. J. Kim, H. N. Hwang and C. C. Hwang, *Appl. Phys. Lett.*, 2007, **91**, 103113.

- 41 A. Thøgersen, S. Diplas, J. Mayandi, T. Finstad, A. Olsen, J. F. Watts, M. Mitome and Y. Bando, *J. Appl. Phys.*, 2008, **103**, 024308.
- 42 A. Thøgersen, J. H. Selj and E. S. Marstein, *J. Electrochem. Soc.*, 2012, **159**, D276.
- 43 G. M. Bancroft, H. W. Nesbitt, R. Ho, D. M. Shaw, J. S. Tse and M. C. Biesinger, *Phys. Rev. B: Condens. Matter Mater. Phys.*, 2009, **80**, 075405.
- 44 Y. R. Choi, M. Zheng, F. Bai, J. Liu, E. Tok, Z. Huang and C.-H. Sow, *Sci. Rep.*, 2014, **4**, 4940.
- 45 A. Shchepetov, M. Prunnila, F. Alzina, L. Schneider, J. Cuffe, H. Jiang, E. I. Kauppinen, C. M. S. Torres and J. Ahopelto, *Appl. Phys. Lett.*, 2013, **102**, 192108.
- 46 C. M. Hessel, J. Wei, D. Reid, H. Fujii, M. C. Downer and B. A. Korgel, *J. Phys. Chem. Lett.*, 2012, **3**, 1089.
- 47 Y. Chen, B. Peng and B. Wang, *J. Phys. Chem. C*, 2007, **111**, 5855.
- 48 M. H. Brodsky, M. Cardona and J. J. Cuomo, *Phys. Rev. B: Solid State*, 1977, **16**, 3556.
- 49 A. S. Kuznetsov, T. Shimizu, S. N. Kuznetsov, A. V. Klekachev, S. Shingubara, J. Vanacken and V. V. Moshchalkov, *Nanotechnology*, 2012, **23**, 475709.
- 50 A. Najjar, A. B. Slimane, M. N. Hedhili, D. Anjum and R. Sougrat, *J. Appl. Phys.*, 2012, **112**, 033502.
- 51 Y. Liu, K. Chen, M. Xiong, P. Zhou, Z. Peng, G. Yang, Y. Cheng, R. Wang and W. Chen, *RSC Adv.*, 2014, **4**, 43760.
- 52 Y. Yang, T. Zhang, L. Le, X. Ruan, P. Fang, C. Pan, R. Xiong, J. Shi and J. Wei, *Sci. Rep.*, 2014, **4**, 7045.
- 53 H. Xu, H. Xiao, H. Pei, J. Cui and W. Hu, *Microporous Mesoporous Mater.*, 2015, **204**, 251.
- 54 M. Anpo, N. Aikawa, Y. Kubokawa, M. Che, C. Louis and E. Giamello, *J. Phys. Chem.*, 1985, **89**, 5017.